AGU PUBLICATIONS

JGR

Journal of Geophysical Research: Space Physics

RESEARCH ARTICLE
10.1002/2016JA023130

Effects of ULF wave power on relativistic radiation belt electrons: 8–9 October 2012 geomagnetic storm

D. Pokhotelov[1], I. J. Rae[1], K. R. Murphy[2], I. R. Mann[3], and L. Ozeke[3]

[1]Mullard Space Science Laboratory, UCL, Dorking, UK, [2]NASA Goddard Space Flight Center, Greenbelt, Maryland, USA, [3]Department of Physics, University of Alberta, Edmonton, Alberta, Canada

Key Points:
- ULF wave behavior is analyzed throughout 8–9 October 2012 geomagnetic storm using multiple satellite missions
- Impact of ULF waves on the transport of radiation belt electrons is quantified by computing radial diffusion coefficients
- The behavior of ULF waves changes throughout the storm from being dominated by compressional waves to being dominated by shear waves

Correspondence to:
D. Pokhotelov,
d.pokhotelov@ucl.ac.uk

Citation:
Pokhotelov, D., I. J. Rae, K. R. Murphy, I. R. Mann, and L. Ozeke (2016), Effects of ULF wave power on relativistic radiation belt electrons: 8–9 October 2012 geomagnetic storm, *J. Geophys. Res. Space Physics*, *121*, 11,766–11,779, doi:10.1002/2016JA023130.

Received 1 JUL 2016
Accepted 18 NOV 2016
Accepted article online 21 NOV 2016
Published online 14 DEC 2016
Corrected 27 JAN 2017

This article was corrected on 27 JAN 2017. See the end of the full text for details.

Abstract Electromagnetic ultralow-frequency (ULF) waves are known to play a substantial role in radial transport, acceleration, and loss of relativistic particles trapped in the Earth's outer radiation belt. Using in situ observations by multiple spacecraft operating in the vicinity of outer radiation belts, we analyze the temporal and spatial behavior of ULF waves throughout the geomagnetic storm of 8–9 October 2012 and compare with the dynamics of relativistic electron fluxes on board the twin Van Allen Probes spacecraft. The analysis shows that the relativistic electron fluxes reduce from their prestorm levels during the first phase of the storm and rapidly increase during the second phase of the storm. We demonstrate that the behavior of ULF wave power changes throughout the storm, from ULF oscillations being a mixture of compressional and shear magnetic components during the first phase of the storm to ULF oscillations being dominated by transverse (shear) components during the second phase. We analyze the parameters of ULF-driven radial diffusion throughout the storm and compare the observed diffusion coefficients with their statistical averages. We demonstrate that the observed diffusion coefficients are strong enough to impact the redistribution of relativistic electron fluxes from and to the outer boundary of radiation belts and the diffusion might influence the effects of any local electron acceleration by transporting fluxes inward or outward according to phase space density gradients.

1. Introduction

The Earth's radiation belts are regions of space where energetic particles (from hundreds of keV to tens of MeV) are trapped by the main magnetic field. The outer belts, peaking at radial distances of 4–5 Earth radii, experience dramatic variability during geomagnetic storms. This variability is governed by a balance of electron acceleration, loss, and transport processes [e.g., *Reeves et al.*, 2003; *Millan and Thorne*, 2007; *Shprits et al.*, 2008a, 2008b]. Mechanisms of relativistic particle energization and loss can be either due to local wave-particle interactions or to radial transport across the magnetosphere. Radial inward transport of radiation belt particles, assisted by storm-enhanced ultralow-frequency (ULF) waves in Pc4 and Pc5 frequency range of 2–22 mHz [*Jacobs et al.*, 1964], may lead to the energization of seed populations of electrons to MeV energies [*Schulz and Lanzerotti*, 1974; *Shprits et al.*, 2008a; *Ozeke et al.*, 2012]. ULF-assisted outward transport and subsequent loss to the magnetopause may lead to rapid depletions of the radiation belts [*Turner et al.*, 2012; *Murphy et al.*, 2015]. Among local mechanisms, acceleration of electrons by gyroresonance interactions with very low frequency (VLF) chorus waves has been long considered as one of the dominant sources of rapid energization [*Summers et al.*, 1998; *Horne et al.*, 2005], though many other local energization and loss mechanism have been invoked. In particular, local acceleration of relativistic electrons by bounce resonance interactions with ULF waves in Pc4 and Pc5 range has been proposed [*Schulz and Lanzerotti*, 1974; *Elkington et al.*, 1999] and confirmed by satellite observations [*Mann et al.*, 2013].

The twin satellite Van Allen Probes mission [*Mauk et al.*, 2013] for the first time provided an opportunity to distinguish between local and radial acceleration/transport processes. *Reeves et al.* [2013] analyzed the evolution of phase space density of relativistic electrons throughout the geomagnetic storm of 8–9 October 2012 and concluded that the sharp increase in ~2 MeV electron fluxes observed in the morning hours of 9 October are due to the local acceleration mechanisms acting outside $L = 4$. *Thorne et al.* [2013] performed numerical simulations of relativistic particle fluxes during this storm (covering the interval from 20 UT 8 October to 12 UT 9 October) suggesting that the local gyroresonance interactions with intense VLF chorus waves observed at consecutive Van Allen Probe orbits throughout the storm could be responsible for the intensification of

electron fluxes in the morning hours of 9 October, while the lack of relativistic electron acceleration during the earlier phase of the storm (not covered by the simulation interval in *Thorne et al.* [2013]) may be attributed to the ULF-enhanced radial transport and subsequent losses to the magnetopause. The role of ULF-enhanced outward transport and magnetopause erosion during this storm has also been emphasized by *Hudson et al.* [2014].

In order to address the question whether the ULF waves should be considered as important drivers of radiation belt dynamics along with VLF chorus and other waves, we examine the behavior of ULF wave power in Pc4 and Pc5 range throughout the 8–9 October 2012 storm, using magnetic field data from two Van Allen Probes, magnetic and electric field data from three Time History of Events and Macroscale Interactions during Substorms (THEMIS) satellites [*Angelopoulos*, 2008] and magnetic field data from three Geostationary Operational Environmental Satellites (GOES) [*Singer et al.*, 1996], and relativistic electron flux data from the Van Allen Probes. Previously the distribution of total power spectral density in time and across magnetic shells has been analyzed during this storm using Van Allen Probes, THEMIS, and GOES data by *Sarris and Li* [2016], who also attempted to reconstruct azimuthal wave numbers of ULF waves. In this study we are focusing on relative behavior of shear and compressional magnetic components and on the comparison of observed radial diffusion coefficients with the statistical averages. The ULF power spectral densities (PSDs) are analyzed in the magnetic field aligned (MFA) coordinates allowing to distinguish between shear and compressional ULF oscillations. Radial diffusion coefficients due to ULF oscillations are computed throughout the storm using magnetic and electric data from the THEMIS probes and magnetic data from the Van Allen Probes. Traditionally, the ULF-driven radial diffusion coefficients are separated into electrostatic and electromagnetic components [e.g., *Schulz and Lanzerotti*, 1974; *Brautigam and Albert*, 2000]. However, it is difficult to separate the electric component of the electric field and the electric field induced by the magnetic fluctuations using the measured electric and magnetic field PSDs (see *Ozeke et al.* [2012] for detailed discussion). In this study we are using the approach proposed by *Brizard and Chan* [2001] and *Fei et al.* [2006] in which the electric (D_{LL}^{E}) and magnetic (D_{LL}^{B}) diffusion coefficients are expressed explicitly in terms of the azimuthal electric field PSD and the field-aligned compressional parallel magnetic field PSD, respectively. The magnitudes of both diffusion coefficients and the change of relative magnitudes D_{LL}^{E}/D_{LL}^{B} are analyzed throughout the storm as a function of time and as a function of magnetic shells. We compare the observed diffusion coefficients with statistical averages as parameterized by *Ozeke et al.* [2014] using *Fei et al.* [2006] formulation.

We analyze the characteristics of ULF waves and demonstrate that ULF power changes substantially throughout the storm, from ULF oscillations being a mixture of compressional and shear magnetic components during the first phase of the storm (from the shock arrival until the arrival of magnetic cloud) to ULF oscillations being dominated by traverse (shear) components during the second phase (until the end of magnetic cloud). We also note that the first phase of the storm is characterized by the reduction in relativistic electron fluxes from prestorm levels, while the second phase is characterized by rapid enhancement in electron fluxes, attributed to the effects of local acceleration by *Reeves et al.* [2013] and *Thorne et al.* [2013]. The analysis of radial diffusion coefficients shows that the magnetic diffusion coefficient D_{LL}^{B} is comparable to or exceeding the statistical averages, while the electric coefficient D_{LL}^{E} is generally below the statistical averages. Still the ratio of diffusion coefficients shows that the electric component is relatively larger and D_{LL}^{E} dominates the diffusion at magnetic shells below $L = 6$ where the Van Allen probes operate. At higher magnetic shells ($L = 6–8$) reached by THEMIS spacecraft, the magnetic component exceeds the electric and thus D_{LL}^{B} can dominate the radial diffusion outside radiation belts. The observed diffusion coefficients are sufficient enough to potentially impact the redistribution of flux from and to the outer boundary and would impact the effects of any local acceleration by transporting flux down phase space density gradients such as examined by *Reeves et al.* [2013].

2. Datasets and Data Processing

2.1. Van Allen Probes Data

The two Van Allen Probes spacecraft operate with varying separation on ~10° inclination orbit with the orbital period of ~9 h and the apogee of ~5.8 Earth radii (R_E). During the storm, the Van Allen Probes A and B operated with the apogees in the dawn magnetic local time (MLT) sector of the magnetosphere (see Figure 1). Six consecutive orbits of the Van Allen Probe A and five consecutive orbits of the Van Allen Probe B are analyzed for this study. The ULF magnetic field data for this study is obtained by the triaxial fluxgate magnetometer which is a part of the Electric and Magnetic Field Instrument Suite and Integrated Science (EMFISIS) experiment [*Kletzing et al.*, 2013]. Level 3 magnetometer data in Geocentric Solar Ecliptic (GSE) coordinates at 4 s

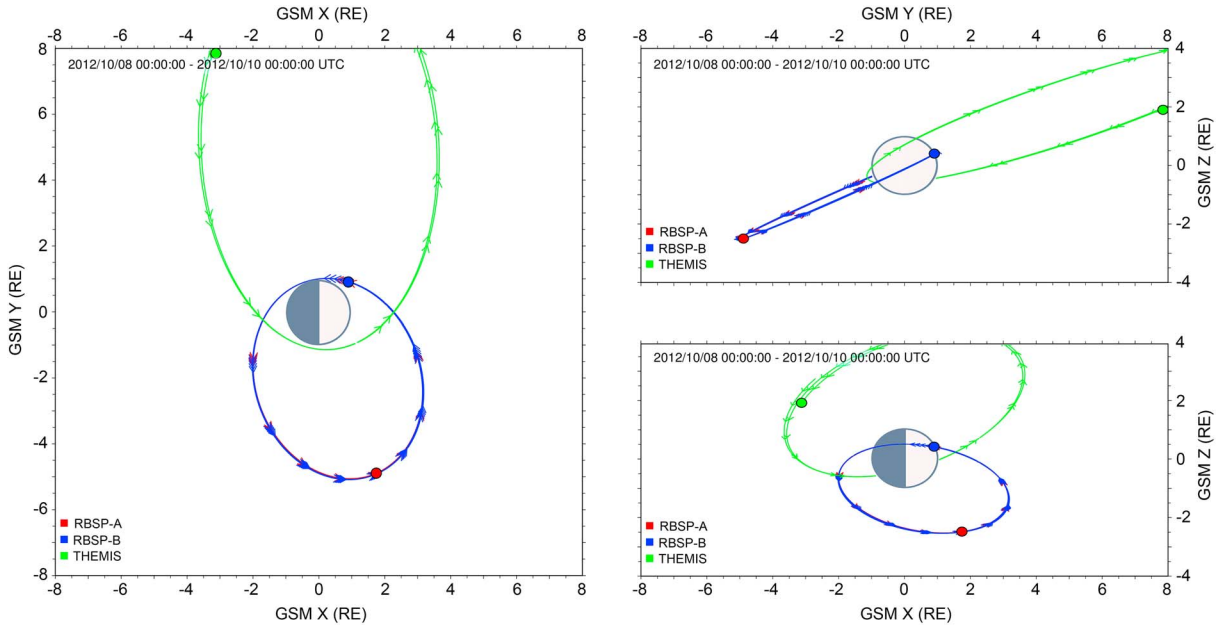

Figure 1. Orbits of the Van Allen Probes A and B and THEMIS probes A, D, and E during 8–9 October 2012 geomagnetic storm.

time resolution have been used for this study. Following approach of *Rae et al.* [2005], the fluxgate magnetometer data have been transformed into orthogonal magnetic field-aligned (MFA) coordinates where the *z* axis is aligned with background magnetic field, the *x* axis is in a plane containing background magnetic field (*z*) and geocentric radius, and the *y* axis completes the right-hand set. The MFA coordinate system is constructed using a background running mean magnetic field estimate of 15 min, and power spectral density (PSD) is calculated for each MFA component using a Morlet wavelet transform.

Due to occasional orbital maneuvers, the Van Allen Probes spacecraft experience quasi-periodic nutations with the frequency of 3.3–3.6 mHz (C. Kletzing, personal communication, 2015) which lasted for 3–4 days after the thruster firings and polluted a part of the ULF frequency band. Such firings took place on 8 October at 13:51 UT and 16:02 UT on Probe A and at 18:32 UT and 20:38 UT on Probe B. To minimize the effects of nutations, the band-stop filtering of the ULF spectra has been applied to remove the affected powers in the range of 2.8–4 mHz. The PSDs of each magnetic component in MFA coordinates are then summed over the frequency range from 1.2 mHz to 20 mHz. This filtering procedure underestimates the total ULF PSDs, but we believe that this represents a more accurate choice than artificially introducing interpolated ULF powers across the polluted frequency band. For the calculation of radial diffusion coefficients, described in section 2.4, the ULF PSDs are linearly interpolated across filtered frequency band to get better representation of the total ULF power for the comparison with statistical parametrizations by *Ozeke et al.* [2014].

To monitor the dynamics of relativistic electrons throughout the storm, spin-averaged differential electron energy flux data from the Relativistic Electron-Proton Telescope (REPT) instrument [*Baker et al.*, 2013] have been analyzed. The level 2 REPT data used in this study are differential energy fluxes of electrons from six energy channels centered at 1.8, 2.1, 2.6, 3.4, 4.2, and 5.2 MeV.

2.2. THEMIS Data

Three of the THEMIS probes (A, D, and E) were operating during this storm with their apogees in the dusk MLT sector of the magnetosphere with the apogee of ~12 R_E (see Figure 1). The magnetic field data for this study are obtained by the triaxial fluxgate magnetometer (FGM) experiment [*Auster et al.*, 2008]. The level 2 magnetometer data in GSE coordinates with 3 s resolution have been used. The electric field data are obtained by the Electric Field Instrument (EFI) [*Bonnell et al.*, 2008] with the level 2 data providing three components of the electric field in GSE coordinates with 3 s resolution derived from the spin plane electric field measurements assuming $E \cdot B = 0$. Following the same procedure as for the Van Allen Probes data, THEMIS magnetic and electric field components have been transformed into MFA coordinates. This transformation leads to a nonzero parallel electric component which is small (order of magnitude) relative to the transverse electric

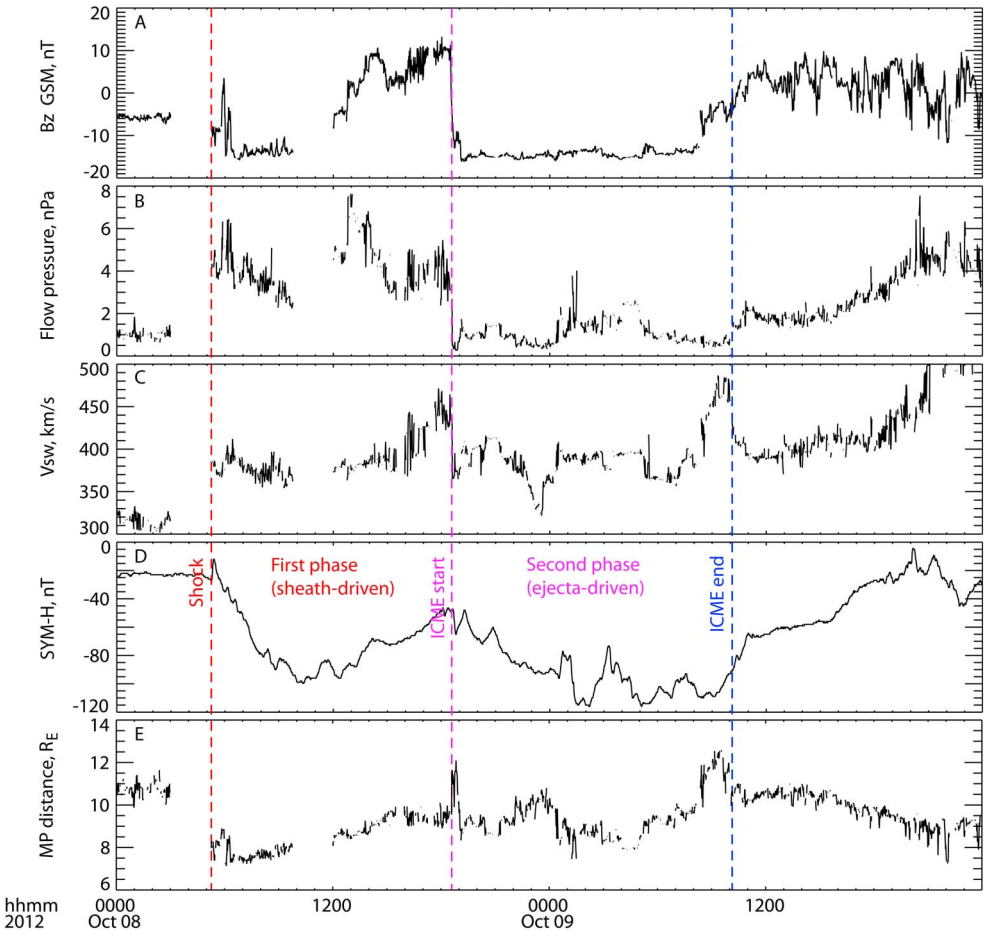

Figure 2. Summary of the 8–9 October 2012 geomagnetic storm: (a) southward component of the interplanetary magnetic field in geocentric solar magnetospheric (GSM) coordinates; (b) solar wind dynamic pressure; (c) solar wind speed; (d) geomagnetic *SYM-H* index; and (e) the location of magnetopause according to *Shue et al.* [1998]. Vertical dashed lines indicate shock arrival, and start and end of the interplanetary coronal mass ejection (ICME) according to *Kilpua et al.* [2015]. Note that the timing of phases has been time shifted to upstream the Earth's bow shock, while the timing in the original work by *Kilpua et al.* [2015] is given in the frame of solar wind monitoring spacecraft.

components and is ignored as an artifact of processing. The PSDs of each magnetic and electric component in MFA coordinates are then summed over the frequency range from 1.2 mHz to 20 mHz.

2.3. GOES Data

GOES data are used here to complement the ULF observations by THEMIS and Van Allen Probes satellites. Data sets of GOES 13, GOES 14, and GOES 15 satellites have been used, with GOES 13 located at the GOES-EAST geostationary orbit slot (357° geomagnetic longitude and 10° geomagnetic latitude), GOES 15 located at the GOES-WEST geostationary orbit slot (296° geomagnetic longitude and 4° geomagnetic latitude), and GOES 14 located in a storage orbit around 332° geomagnetic longitude and 9° geomagnetic latitude. The ULF magnetic field data for this study are obtained by the triaxial fluxgate magnetometer (FGM) experiment [*Singer et al.*, 1996]. The FGM data with 512 ms resolution have been downsampled to 4 s resolution and transformed from spacecraft's own coordinates (*p*, *e*, *n*) into MFA coordinates.

2.4. Radial Diffusion Coefficients

Following *Ozeke et al.* [2014], the magnetic (D_{LL}^{B}) and electric (D_{LL}^{E}) radial diffusion coefficients are expressed analytically in terms of compressional magnetic field PSD $B_{\|}$ and azimuthal electric field PSD E_{ϕ} as

$$D_{LL}^{B} = \frac{4\pi^2}{9 \times 8B_E^2} L^8 B_{\|}, \quad (1)$$

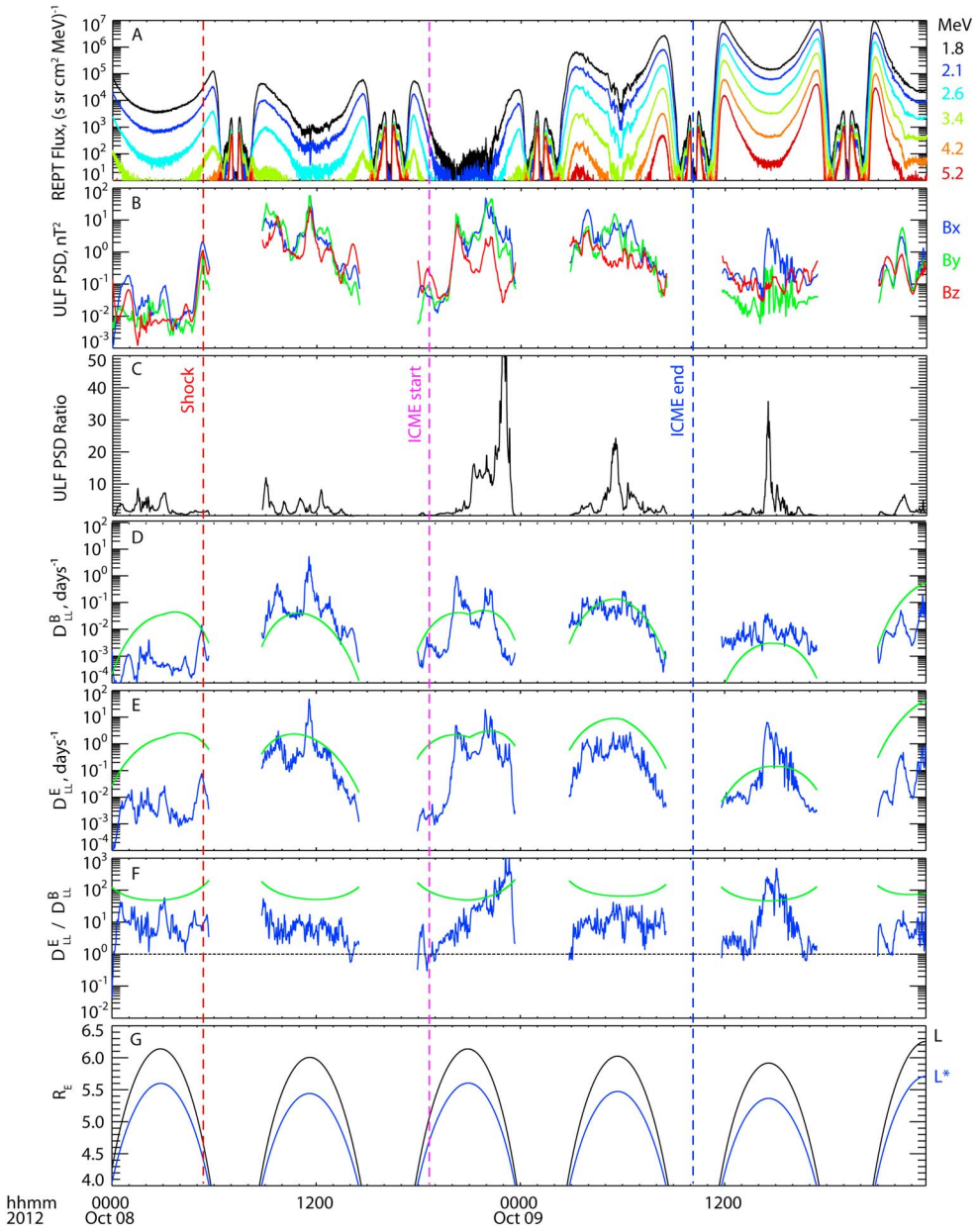

Figure 3. Summary of the Van Allen Probe A data: (a) spin-averaged differential electron fluxes from the REPT instrument; (b) the sums of ULF PSD in each magnetic field component; (c) the ratio of ULF PSD in transverse and parallel magnetic components; (d) magnetic radial diffusion coefficients; (e) electric radial diffusion coefficients; (f) ratio of the radial diffusion coefficients; and (g) magnetic shells. In Figures 3d–3f blue and green curves indicate measured diffusion coefficients and statistical parametrizations, respectively. Vertical dashed lines indicate shock arrival, and start and end of the ICME.

$$D^E_{\mathrm{LL}} = \frac{1}{8B_E^2R_E^2}L^6E_\phi, \tag{2}$$

where B_E denotes the equatorial magnetic field strength at the surface of the Earth, $E_\phi = \langle \mathrm{PSD}(E_y)\rangle$ is the mean ULF power in the azimuthal electric field component, and $B_\parallel = \langle \mathrm{PSD}(B_z)f^2\rangle$ is the mean ULF power in the compressional magnetic field component multiplied by the squared frequency f of each spectral component. The statistical averages of magnetic and electric diffusion coefficients for given geomagnetic conditions as a function of L shell and 3 h global geomagnetic activity index K_p are parameterized by *Ozeke et al.* [2014] (in units of day^{-1}) as

$$D^B_{\mathrm{LL}} = 6.62\times10^{-13}L^8 10^{-0.0327L^2+0.625L-0.0108K_p^2+0.499K_p}, \tag{3}$$

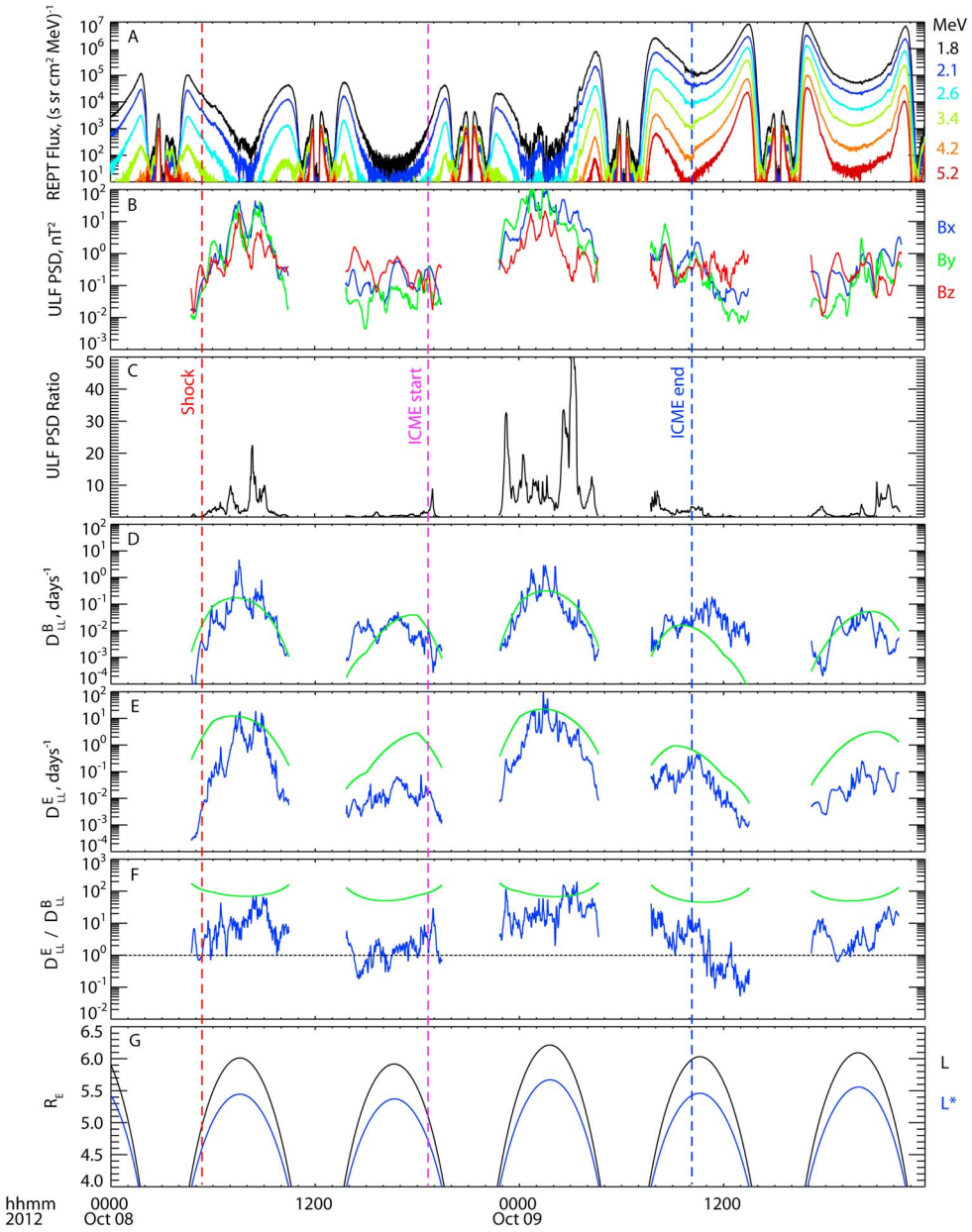

Figure 4. Summary of the Van Allen Probe B data: (a) spin-averaged differential electron fluxes from the REPT instrument; (b) the sums of ULF PSD in each magnetic field component; (c) the ratio of ULF PSD in transverse and parallel magnetic components; (d) magnetic radial diffusion coefficients; (e) electric radial diffusion coefficients; (f) ratio of the radial diffusion coefficients; and (g) magnetic shells. In Figures 4d–4f blue and green curves indicate measured diffusion coefficients and statistical parametrizations, respectively. Vertical dashed lines indicate shock arrival, and start and end of the ICME.

$$D^E_{\mathrm{LL}} = 2.16 \times 10^{-8} L^6 10^{0.217L+0.461K_p}. \quad (4)$$

Note that the diffusion coefficients in *Ozeke et al.* [2014] are parameterized using McIlwain magnetic shell parameter [*McIlawin*, 1961], while the analysis of electron phase space densities in *Reeves et al.* [2013] is presented using Roederer magnetic shell parameter [*Roederer*, 1970]. Thus, throughout this paper both parameters are used, marked as L and $L^\star$, respectively.

Magnetic and electric diffusion coefficients are computed for the three THEMIS probes using measured ULF PSDs of compressional magnetic component (B_z) and azimuthal electric component (E_y), respectively. Since the ULF electric field data are not available for the Van Allen Probes during this storm due to spacecraft

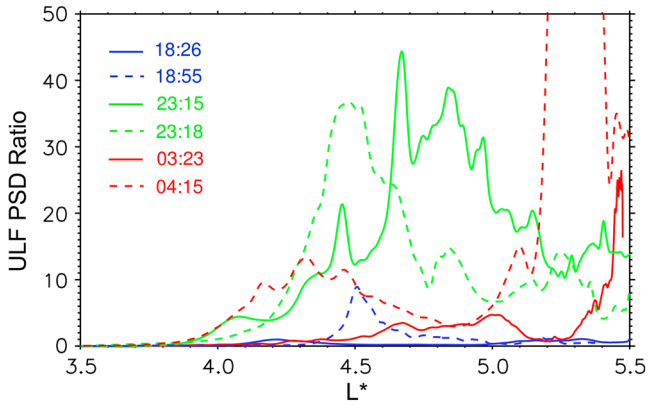

Figure 5. The ratio of ULF PSD in transverse and parallel components as a function of $L^\star$ for six consecutive outbound/inbound passes of Van Allen Probes between 18 UT 8 October and 04 UT 9 October. Solid and dashed lines correspond to Probes A and B, respectively. The times (in UT) indicate the moments when the respective probe crosses $L^\star = 4.5$.

charging events (J. Wygant, personal communication, 2015), the PSD of azimuthal electric component (E_y) is inferred from the PSD of radial magnetic component (B_x) measured by the Van Allen Probes. To achieve this, the mean ratio of ULF PSDs in E_y and B_x components is computed from electric and magnetic data measured by one of the THEMIS probes (Probe E) located in a different MLT sector but on the same L shells as the Van Allen Probe A. To compute the ratio, the THEMIS ULF PSD data are averaged over $L = 4.2–6.0$ (corresponding to geomagnetic latitudes GMLat = −4.5° to −6.3° and to the time interval 03:42–04:42 UT 9 October). During this UT interval, the Van Allen Probe A was located around $L = 5$ and GMLat = −3°. The ratio of ULF PSDs is then used to infer the electric diffusion coefficients for the Van Allen Probes data set.

3. An Overview of 8–9 October 2012 Geomagnetic Storm

The ICME-driven geomagnetic storm commenced on 8 October following the arrival of interplanetary shock around 05:15 UT. The storm is characterized by a double dip in the *SYM-H* geomagnetic activity index, associated with two extended periods of southward interplanetary magnetic field (IMF) orientation (see Figure 2). Solar wind and IMF parameters are provided by the Operating Missions as a Node on the Internet (OMNI) database using the Advanced Composition Explorer and Wind spacecraft data, generated from 1 to 4 min resolution data time shifted to upstream the Earth's bow shock [*King and Papitashvili*, 2005]. The storm's main phase demonstrates clear two-phase structure, with the first phase (from 05:15 to 18:40 UT 8 October) corresponding to the sheath interval and the second phase (lasting until 10:10 UT 9 October) corresponding to the ejecta interval as identified by *Kilpua et al.* [2015].

In terms of interplanetary drivers the storm has been classified as S3 type [*Kilpua et al.*, 2015], i.e., demonstrating clear geoeffective sheath and ejecta intervals. Commonly, the main phase of ICME-driven storms is associated with southward IMF interval during the ejecta, accompanied by the negative excursion of *SYM-H* index, but since both sheath and ejecta intervals have extended periods of southward IMF, this storm can be described as two-step main phase storm [e.g., *Tsurutani and Gonzalez*, 1994], with the sheath- and ejecta-driven intervals composing the main phase and the recovery phase starting after 10 UT 9 October. While the ejecta is characterized by extended period of southward IMF and largely free of ULF oscillations, the sheath is characterized by compressed hot plasma accompanied by high fluctuation levels in ULF Pc4 and Pc5 frequency range [*Tsurutani and Gonzalez*, 1994]. Throughout this article we address the sheath-driven interval of the storm's main phase as the "first phase" and the ejecta-driven interval of the main phase as the "second phase."

The differential electron energy fluxes and the characteristics of ULF wave power throughout the storm are summarized in Figures 3 and 4 for the Van Allen Probes A and B, respectively. The fluxes of relativistic MeV electrons (Figures 3a–4a) show a decrease (from prestorm levels) during the first phase of the storm, followed by sharp increase (2–3 orders of magnitude) during the second phase of the storm, particularly during the interval 22 UT 8 October to 04 UT 9 October. After the sharp increase, the electron fluxes stay at high levels followed by slow reduction after the end of the storm's main phase.

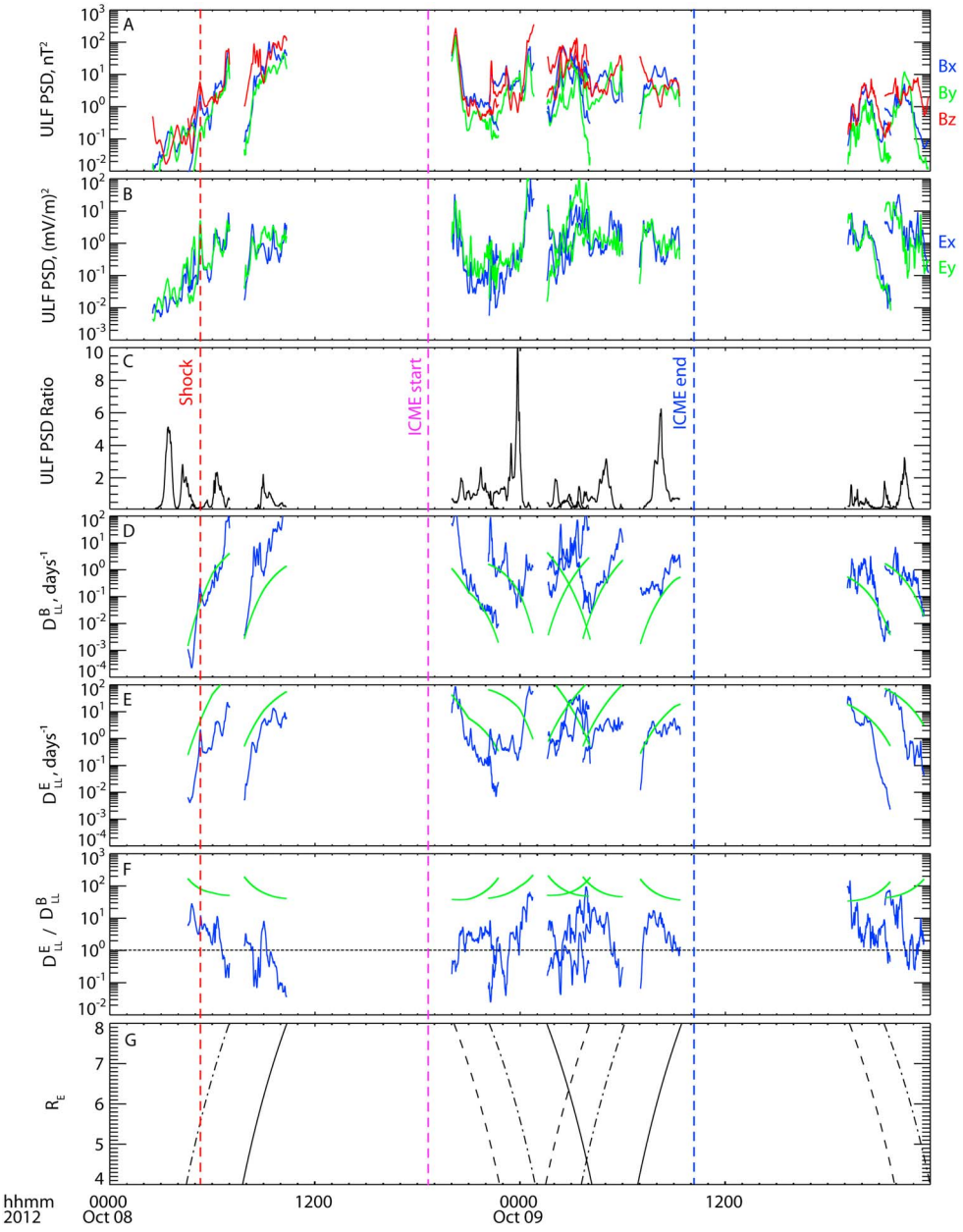

Figure 6. Summary of the three THEMIS probes data: (a) the sums of ULF PSD in each magnetic field component; (b) the sums of ULF PSD in each electric component; (c) the ratio of ULF PSD in transverse and parallel magnetic components; (d) magnetic radial diffusion coefficients; (e) electric radial diffusion coefficients; (f) ratio of the radial diffusion coefficients; and (g) magnetic shells. In Figures 6d–6f blue and green curves indicate measured diffusion coefficients and statistical parametrizations, respectively. Vertical dashed lines indicate shock arrival, and start and end of the ICME.

The sums of ULF PSD in each magnetic component (B_x, B_y, and B_z) are shown as line plots in Figures 3b and 4b. The ULF PSDs increase sharply (2–3 orders of magnitude) following the shock arrival, and the total ULF power stays elevated during the first dip of *SYM-H* index (the first phase), then decreases during the post-noon period of 8 October, increases again (2 orders of magnitude) during the second dip of *SYM-H* index (the second phase), and decreases during the recovery phase. Thus, the total ULF PSD is increased during the first phase and during the second phase, while the electron fluxes are reduced during the first phase and increased during the second phase.

However, the nature of ULF fluctuations differs substantially from the first to the second phase of the storm. During the first phase, the ULF power in radial (B_x) and azimuthal (B_y) components of the magnetic

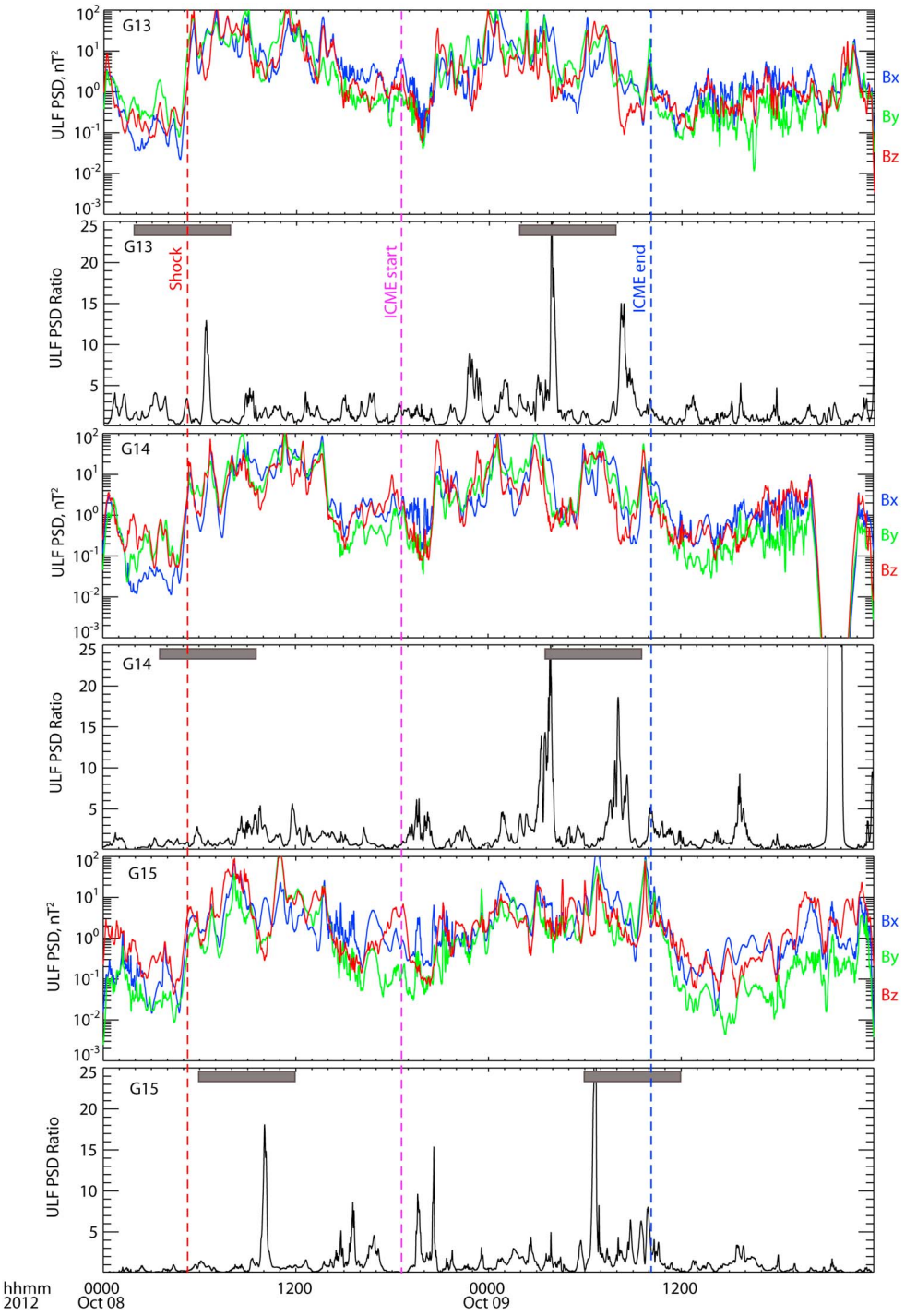

Figure 7. Sums of ULF power in each magnetic field component and the ratios of ULF PSD in transverse and parallel components measured by GOES 13, GOES 14, and GOES 15 spacecraft. Horizontal gray bars indicate intervals when GOES is located in the night sector (21–03 MLT). Zero values of ULF PSD and infinite values of ULF PSD Ratio around 21–22 UT seen on GOES 14 correspond to the gap in FGM data. Vertical dashed lines indicate shock arrival, and start and end of the ICME.

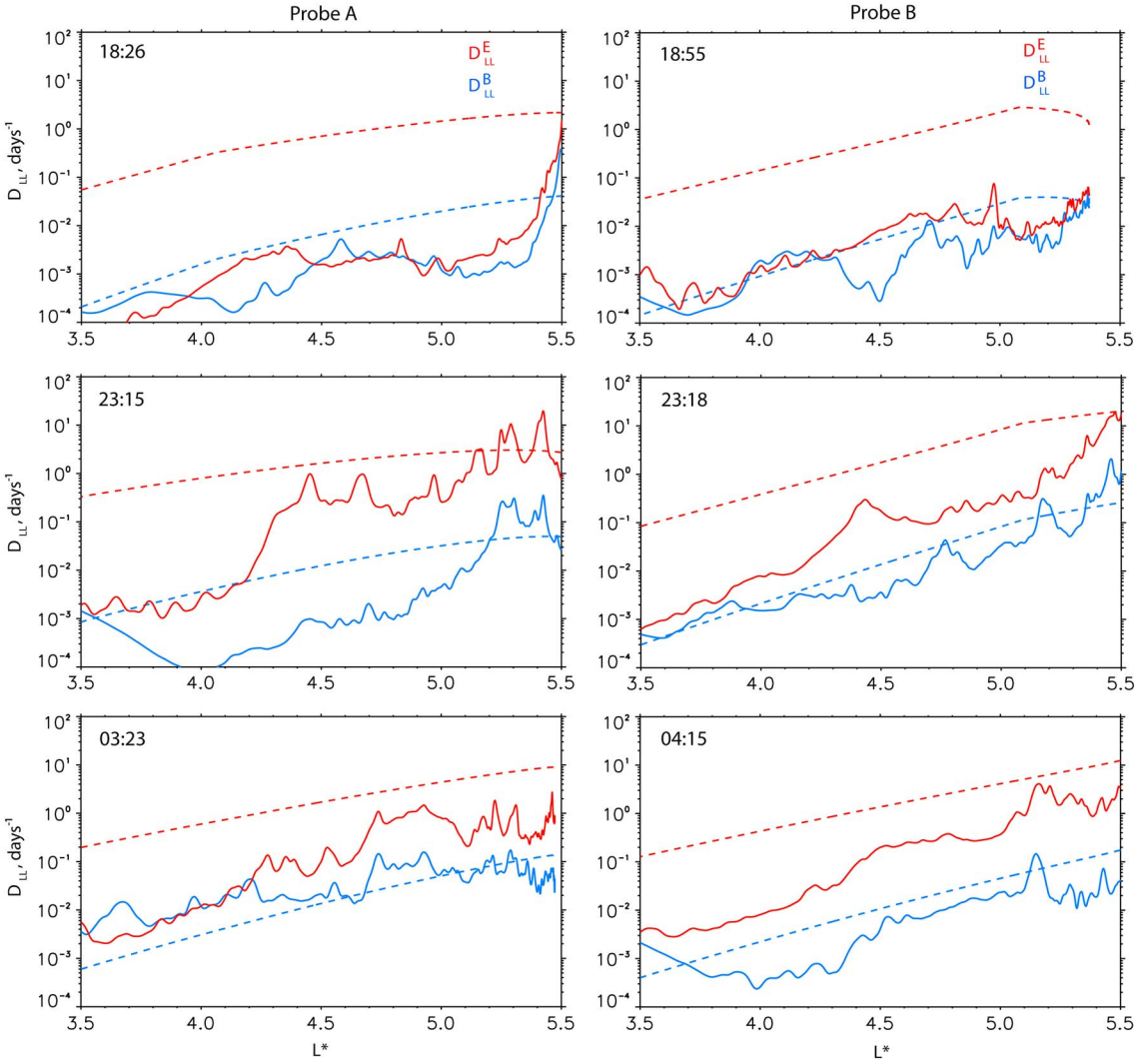

Figure 8. Radial diffusion coefficients as a function of $L^\star$ for six consecutive outbound/inbound passes of Van Allen Probes between 18 UT 8 October and 04 UT 9 October. (left and right columns) Probes A and B, respectively. Solid lines show the diffusion coefficients derived/inferred from Van Allen Probes magnetic measurements; dashed lines show the statistical values of diffusion coefficients parameterized by *Ozeke et al.* [2014]. Blue/red color corresponds to electric/magnetic diffusion terms. The times (in UT) indicate the moments when the respective probe crosses $L^\star = 4.5$.

perturbations largely resembles the behavior of ULF power in parallel (B_z) component. During the second phase of the storm, the ULF power in two transverse components (B_x and B_y) substantially exceeds the ULF power in parallel (B_z) component. This difference in ULF power between transverse and parallel components is most noticeable during late evening of 8 October and early morning of 9 October, specifically during 20–24 UT 8 October on Van Allen Probe A (Figure 3) and 23 UT 8 October to 05 UT 9 October on Van Allen Probe B (Figure 4). To better illustrate the change in ULF behavior, the ratio of ULF PSDs in transverse and parallel components, defined as $0.5(\mathrm{PSD}(B_x)+\mathrm{PSD}(B_y))/\mathrm{PSD}(B_z)$, is shown in Figures 3c and 4c. The ratio of ULF power is also presented in Figure 5 as a function of $L^\star$ for six consecutive (inward and outward) Van Allen Probe passes through the outer belt region ($L^\star = 3.5–5.5$) during the interval 18 UT 8 October to 04 UT 9 October. The ULF PSD ratio increases dramatically from the two passes around 18 UT 8 October (blue lines) to the passes around 23 UT 8 October (green lines) and stays elevated at the passes around 03–04 UT 9 October (red lines).

The sums of ULF power in three magnetic (B_x, B_y, and B_z) and two electric (E_x and E_y) components measured by THEMIS probes A, D, and E during two consecutive orbits on 8–9 October are summarized in Figures 6a and 6b. THEMIS data also show sharp increase in ULF power following the shock arrival and another increase in ULF power around the second dip in *SYM-H* index in the late night-early morning hours of 8–9 October.

The ULF power in magnetic components have two maxima during the storm's phase at 08–11 UT 8 October and during the second phase at 00–05 UT 9 October. In contrast, the ULF power in two electric components have maximum values during the second phase at 00–05 UT 9 October. The ratio of ULF power between transverse and parallel components, computed in the same way as for Van Allen Probes, is shown in Figure 6c. Clearly, on THEMIS, the change in ULF behavior between first and second phases of the storm is less pronounced comparing to the Van Allen Probes data. The ULF PSD ratio maximizes during the storm's second phase around 00 UT 9 October (consistently with the Van Allen Probes), coinciding with the maximum values of ULF power in two electric components.

Figure 7 shows the sums of ULF power in three magnetic (B_x, B_y, and B_z) components measured by geostationary GOES 13, GOES 14, and GOES 15 spacecraft throughout the storm, as well as the ratios of ULF PSD in transverse and parallel components for each GOES spacecraft. Zero values of ULF PSD seen on GOES 14 around 21–22 UT 9 October correspond to the gap in FGM data. As with other data sets, the sharp increase in ULF power is seen after the shock arrival and the ULF power stays elevated throughout the storm. The behavior of ULF PSD ratios is more consistent between GOES 13 and GOES 14 spacecraft and somewhat differs on GOES 15. Yet all three GOES spacecraft show the highest values of ULF PSD ratio during the second phase of the storm, with the ratios peaking around 04 UT and 08 UT 9 October on GOES 13 and GOES 14 and around 06:30 UT on GOES 15.

For three THEMIS probes, the magnetic and electric diffusion coefficients are presented in Figures 6d and 6e, with blue lines showing measured values of the diffusion rates computed using equations (1) and (2) and green lines showing the statistical averages of diffusion coefficients given by equations (3) and (4). Figure 6f shows the ratios between electric and magnetic diffusion coefficients, based on measured PSD values (blue lines) and on statistical averages (green lines). The magnetic and electric diffusion coefficients for the Van Allen Probes A and B are summarized in (blue lines) of Figures 3d and 3 and 4d and 4f (blue lines). The statistical averages of diffusion coefficients are shown by green lines in Figures 3d and 3 and 4d and 4f.

The interval of 18 UT 8 October to 04 UT 9 October is of particular interest as previous studies identified local enhancements in electron space phase densities around $L^\star = 4.5$ [*Reeves et al.*, 2013; *Thorne et al.*, 2013]. To analyze the behavior of radial transport in this interval, the magnetic and electric diffusion coefficients are presented in Figure 8 as a function of $L^\star$ for six consecutive inward and outward Van Allen Probe passes. The statistical averages of diffusion coefficients are also shown as a function of $L^\star$ for comparison.

4. Discussion

The rapid enhancement of relativistic electron fluxes during the interval 23 UT 8 October to 04 UT 9 October 2012 has been previously described by *Reeves et al.* [2013] who attributed the flux enhancement to local acceleration mechanisms acting to increase the phase space densities locally. While *Reeves et al.* [2013] did not identify a specific mechanism of local electron acceleration, *Thorne et al.* [2013] suggested that the intense VLF chorus emissions observed throughout the storm could be the main source of local acceleration of relativistic electrons. To emphasize the point, *Thorne et al.* [2013] performed a numerical simulation of electron fluxes throughout the later phase of the storm (starting the simulation at 20 UT 8 October). The first-principle Fokker-Plank simulation was based on the model of gyroresonance interactions between VLF chorus waves and relativistic electrons, coupled with a data-driven model of chorus wave intensity. The simulation results suggested that the VLF chorus waves can act as a mechanism of local electron acceleration during the simulated phase of the storm, but it did not explain the lack of relativistic flux enhancement during the earlier phase of the storm, when intense chorus waves are also present. *Thorne et al.* [2013] suggested that the reduction of MeV electron fluxes in the first phase of the storm can be associated with rapid ULF-enhanced outward diffusion of accelerated electrons and subsequent loss to the magnetopause. The detailed analysis of ULF-enhanced diffusion during this storm is presented below.

The analysis of THEMIS probes (Figure 6) indicates that the magnetic diffusion coefficients D_{LL}^{B} are highest during the first phase of the storm, substantially (1–2 orders of magnitude) exceeding the statistical averages, particularly at higher L shells. During this first phase the magnetic diffusion terms dominate over the electric terms, as evidenced by the ratios shown in Figure 6f. The second phase is characterized by the enhanced electric diffusion terms D_{LL}^{E}, reaching, or exceeding, the statistical averages. In particular, the interval 00–06 UT 9 October is dominated by the electric term, as evidenced by the ratios of diffusion coefficients.

Similar to THEMIS probes, the magnetic diffusion coefficients observed by Van Allen Probes (Figures 3 and 4) are highest during the first phase of the storm, exceeding the statistical averages by 1–2 orders of magnitude at highest L shells. During the second phase the D_{LL}^{B} terms are lower relative to the first phase and on the same level with the statistical averages, on both Van Allen Probes A and B. The electric D_{LL}^{E} coefficients are generally higher during the second phase of the storm (especially in the interval 22 UT 8 October to 04 UT 9 October), and the ratio D_{LL}^{E}/D_{LL}^{B} indicates the second phase to be dominated by the electric diffusion terms. However, we need to be careful in interpreting the electric diffusion coefficients on Van Allen Probes, as they are inferred from the radial magnetic component (B_x) with the use of E_y/B_x ratio measured by THEMIS. Radial profiles of the diffusion coefficients shown as a function L^* for the Van Allen probe passes in the interval 18 UT 8 October to 04 UT 9 October (Figure 8) indicate that on most of these passes both D_{LL}^{B} and D_{LL}^{E} are reduced relative to statistical averages in the center of outer radiation belts ($L^* = 4–5$) and increased relative to statistical averages at higher magnetic shells ($L^* > 5$).

The time interval where *Reeves et al.* [2013] identified the local electron acceleration coincides with the enhancement of ULF power on the corresponding parts of Van Allen Probe A orbit (22–24 UT 8 October) and Probe B orbit (00–04 UT 9 October). Moreover, starting from 22 UT 8 October, we observe change in the behavior of ULF waves with the power in two transverse magnetic components (B_x and B_y) substantially exceeding the power in parallel component (B_z). This may indicate favorable conditions for coherent interactions with electrons, as the enhanced ULF power in radial magnetic component is expected to enhance ULF power in azimuthal electric fields. While this cannot be confirmed without analyzing the electric field data on Van Allen Probes, unavailable for this storm, the ULF power in azimuthal and radial electric field components measured by THEMIS appears to maximize in approximately the same time interval, suggesting favorable conditions for coherent interactions.

The change in the behavior of ULF power, from mixed/compressional during the first phase of the storm to mainly shear dominant during the second phase, is clearly seen by Van Allen Probes in the dawn MLT sector, however is less pronounced on THEMIS probes crossing the same range of L shells in the dusk MLT sector. The maximum ULF PSD ratio is seen on THEMIS probes around 00 UT 9 October (Figure 6) that is roughly coincident with the main peak of ULF PSD ratios observed by Van Allen Probe A (Figure 3) and the first of two main peaks observed by Van Allen Probe B (Figure 4). One has to take into account that due to their orbits, THEMIS probes cross the outer belts region between $L = 4$ and 6 approximately 3 times faster ($\sim$1 h versus $\sim$ 3 h) comparing to Van Allen Probes; thus, the change in ULF behavior could be less evident or missing in THEMIS data. The difference in ULF behavior between THEMIS and Van Allen Probes may also be related to the dawn-dusk asymmetries (see discussion below), but such asymmetries need to be properly addressed in a statistical study. The behavior of ULF PSD ratio seen on GOES 13 to GOES 15 spacecraft (Figure 7) is also generally consistent with the conclusion that ULF power changes from compressional to shear dominant between the first and second phases of the storm. However, the ULF PSD ratio observed by GOES spacecraft needs to be interpreted carefully as sudden changes in magnetic field due to nightside dipolarizations and substorm activity can also affect ULF power. In Figure 7 the intervals when GOES spacecraft is located in the night MLT sector (21–03 MLT) are marked with horizontal gray bars.

The observed change in the behavior of ULF waves between the first and second phases of the storm allows few possible interpretations. (a) The ULF oscillations during the first phase of the storm are observed in the region closer to the magnetopause; thus, the predominantly compressional ULF waves penetrating through the magnetopause are less likely to be converted into coherent ULF waves associated with local field line eigenmodes. (b) The penetration of ULF waves through the magnetopause is fundamentally different between the two phases of the storm, with the first phase of the storm (associated with turbulent sheath interval with high levels of ULF perturbations) is more likely to produce incoherent mostly compressional ULF waves, while the second phase (associated with much less turbulent ejecta interval, mostly free of ULF perturbations) is more likely to produce more coherent shear-dominant ULF signatures. Both interpretations require more observations through different phases of other storms focusing on: (a) the location of ULF observations relative to the magnetopause and (b) the internal structure of ICME, in particular, other S3 type storms with clear geoeffective sheath and ejecta intervals.

Earlier statistical studies reported asymmetries between dawn and dusk sectors in the ULF wave power as well as in the occurrence of ULF Pc4 and Pc5 pulsations. Such asymmetries need to be considered when inferring the electric field power on the Van Allen Probes in the dawn sector from THEMIS observations in the dusk

sector. Based on the analysis of THEMIS data, *Liu et al.* [2010] suggested that the average magnitudes of Pc4 and Pc5 pulsations are higher in the dusk sector relative to the dawn sector for all three magnetic field components and for two electric field components [see *Liu et al.*, 2010, Figure 1]. However, when the statistical data set is binned into sectors in radial distance and local time [*Liu et al.*, 2009], it becomes evident that the largest dawn-dusk asymmetries in wave magnitudes are confined to large radial distances (7–9 R_E), while at the radial distances considered in our study (4–6 R_E) the dawn-dusk asymmetries become marginal [see *Liu et al.*, 2009, Figure 8], especially for the azimuthal electric field component that is considered in our calculations of the diffusion coefficients. Reconstructions of ULF Pc4 and Pc5 electric wave power using ground-based magnetic observations at the footprints of various magnetic shells [*Rae et al.*, 2012] also suggest higher power in both radial and azimuthal electric field in the dusk sector relative to the dawn. However, similar to the in situ observations by *Liu et al.* [2009], the largest dawn-dusk asymmetries appear at higher L shells ($L > 7$), while at $L = 4–6$ studied here the dawn-dusk asymmetries become less pronounced. Thus, we ignore a potential impact of the dawn-dusk asymmetries on the reconstruction of electric field power at lower L shells.

5. Summary and Conclusions

The behavior of ULF Pc4 and Pc5 waves and relativistic electron fluxes across outer radiation belts during 8–9 October 2012 ICME-driven storm is analyzed using combined data sets of two Van Allen Probes, three THEMIS probes, and three GOES satellites. Magnetic and electric radial diffusion coefficients associated with ULF waves are derived from THEMIS electric and magnetic observations. The magnetic radial diffusion coefficients are also derived from the Van Allen Probes magnetic observations, and the electric diffusion coefficients are inferred using a combination of THEMIS and Van Allen Probes data. The statistical estimates of radial diffusion coefficients are done using *Ozeke et al.* [2014] parametrizations. The following conclusions are made:

1. The characteristics of observed ULF waves change throughout the storm from being a mixture of shear and compressional components during the first phase to being shear dominated during the second phase of the storm.
2. The first phase (associated with net reduction in relativistic electron fluxes) is characterized by the enhanced radial diffusion due to the compressional magnetic component, with the magnetic diffusion term D^B_{LL} exceeding the statistical averages by 1–2 orders, particularly at higher L shells, as seen by THEMIS. This may contribute to the reduction of electron fluxes due to radial outward transport and loss to the magnetopause.
3. The second phase (associated with relativistic flux enhancement) is characterized by the enhanced diffusion due to the azimuthal electric field component. In particular, the early interval of the ejecta (22 UT 8 October to 05 UT 9 October) is dominated by the electric diffusion term D^E_{LL} (as observed directly by THEMIS and inferred from Van Allen Probes data), with D^E_{LL} values close to, or above, the statistical averages. This may indicate an important role for ULF wave transport, and potentially acceleration, during the period of the electron flux enhancement, perhaps in addition to or acting in concert with the effects of local VLF chorus electron acceleration identified during this interval by *Thorne et al.* [2013].

Acknowledgments
D.P. and I.J.R. are supported by Science and Technology Facilities Council (STFC) grants ST/L000563/1 and ST/N000722/1. K.R.M. is partially supported by a Canadian NSERC postdoctoral fellowship. The Van Allen Probes EMFISIS fluxgate magnetometer data, the list of spacecraft charging events, and the list of spacecraft maneuver events are provided by the University of Iowa (https://emfisis.physics.uiowa.edu). The Van Allen Probes REPT and MagEIS particle data are provided by the Los Alamos National Laboratory (https://www.rbsp-ect.lanl.gov). THEMIS FGM and EFI data are provided by the University of California, Berkeley (https://themis.ssl.berkeley.edu). GOES FGM data are provided by the NOAA's National Centers for Environmental Information (https://ngdc.noaa.gov). Solar wind data and geomagnetic indices are obtained from NASA OMNIWeb (https://omniweb.gsfc.nasa.gov). We acknowledge the use of Space Physics Environment Data Analysis Software (SPEDAS) suite.

References

Angelopoulos, V. (2008), The THEMIS mission, *Space Sci. Rev.*, *141*, 5–34, doi:10.1007/s11214-008-9336-1.

Auster, H. U., et al. (2008), The THEMIS fluxgate magnetometer, *Space Sci. Rev.*, *141*, 235–264, doi:10.1007/s11214-008-9365-9.

Baker, D. N., et al. (2013), The Relativistic Electron-Proton Telescope (REPT) instrument on board the Radiation Belt Storm Probes (RBSP) spacecraft: Characterization of Earth's radiation belt high-energy particle populations, *Space Sci. Rev.*, *179*, 337–381, doi:10.1007/s11214-012-9950-9.

Bonnell, J. W., F. S. Mozer, G. T. Delory, A. J. Hull, R. E. Ergun, C. M. Cully, V. Angelopoulos, and P. R. Harvey (2008), The Electric Field Instrument (EFI) for THEMIS, *Space Sci. Rev.*, *141*, 303–341, doi:10.1007/s11214-008-9469-2.

Brautigam, D. H., and J. M. Albert (2000), Radial diffusion analysis of outer radiation belt electrons during the October 9, 1990 magnetic storm, *J. Geophys. Res.*, *105*, 291–309, doi:10.1029/1999JA900344.

Brizard, A. J., and A. A. Chan (2001), Relativistic bounce-averaged quasilinear diffusion equation for low-frequency electromagnetic fluctuations, *Phys. Plasmas*, *8*(11), 4762–4771, doi:10.1063/1.1408623.

Elkington, S. R., M. K. Hudson, and A. A. Chan (1999), Acceleration of relativistic electrons via drift resonant interactions with toroidal-mode Pc-5 ULF oscillations, *Geophys. Res. Lett.*, *26*, 3273–3276, doi:10.1029/1999GL003659.

Fei, Y., A. A. Chan, S. R. Elkington, and M. J. Wiltberger (2006), Radial diffusion and MHD particle simulations of relativistic electron transport by ULF waves in the September 1998 storm, *J. Geophys. Res.*, *111*, A12209, doi:10.1029/2005JA011211.

Horne, R. B., et al. (2005), Wave acceleration of electrons in the Van Allen radiation belts, *Nature*, *437*, 227–230, doi:10.1038/nature03939.

Hudson, M. K., D. N. Baker, J. Goldstein, B. T. Kress, J. Paral, F. R. Toffoletto, and M. Wiltberger (2014), Simulated magnetopause losses and Van Allen Probe flux dropouts, *Geophys. Res. Lett.*, *41*, 1113–1118, doi:10.1002/2014GL059222.

Jacobs, J. A., Y. Kato, S. Matsushita, and V. A. Troitskaya (1964), Classification of geomagnetic micropulsations, *J. Geophys. Res.*, *69*, 180–181, doi:10.1029/JZ069i001p00180.

Kilpua, E. K. J., H. Hietala, D. L. Turner, H. E. J. Koskinen, T. I. Pulkkinen, J. V. Rodriguez, G. D. Reeves, S. G. Claudepierre, and H. E. Spence (2015), Unraveling the drivers of the storm time radiation belt response, *Geophys. Res. Lett.*, *42*, 3076–3084, doi:10.1002/2015GL063542.
King, J. H., and N. E. Papitashvili (2005), Solar wind spatial scales in and comparisons of hourly Wind and ACE plasma and magnetic field data, *J. Geophys. Res.*, *110*, A02104, doi:10.1029/2004JA010649.
Kletzing, C. A., et al. (2013), The Electric and Magnetic Field Instrument Suite and Integrated Science (EMFISIS) on RBSP, *Space Sci. Rev.*, *179*, 127–181, doi:10.1007/s11214-013-9993-6.
Liu, W., T. E. Sarris, X. Li, S. R. Elkington, R. Ergun, V. Angelopoulos, J. Bonnell, and K. H. Glassmeier (2009), Electric and magnetic field observations of Pc4 and Pc5 pulsations in the inner magnetosphere: A statistical study, *J. Geophys. Res.*, *114*, A12206, doi:10.1029/2009JA014243.
Liu, W., T. E. Sarris, X. Li, R. Ergun, V. Angelopoulos, J. Bonnell, and K. H. Glassmeier (2010), Solar wind influence on Pc4 and Pc5 ULF wave activity in the inner magnetosphere, *J. Geophys. Res.*, *115*, A12201, doi:10.1029/2010JA015299.
Mann, I. R., et al. (2013), Discovery of the action of a geophysical synchrotron in the Earth's Van Allen radiation belts, *Nat. Commun.*, *4*, 2795, doi:10.1038/ncomms3795.
Mauk, B. H., N. J. Fox, S. G. Kanekal, R. L. Kessel, D. G. Sibeck, and A. Ukhorskiy (2013), Science objectives and rationale for the radiation belt storm probes mission, *Space Sci. Rev.*, *179*, 3–27, doi:10.1007/s11214-012-9908-y.
McIlwain, C. E. (1961), Coordinates for mapping the distribution of magnetically trapped particles, *J. Geophys. Res.*, *66*, 3681–3691, doi:10.1029/JZ066i011p03681.
Millan, R. M., and R. M. Thorne (2007), Review of radiation belt relativistic electron losses, *J. Atmos. Sol. Terr. Phys.*, *69*, 362–377, doi:10.1016/j.jastp.2006.06.019.
Murphy, K. R., I. R. Mann, and D. G. Sibeck (2015), On the dependence of storm time ULF wave power on magnetopause location: Impacts for ULF wave radial diffusion, *Geophys. Res. Lett.*, *42*, 9676–9684, doi:10.1002/2015GL066592.
Ozeke, L. G., I. R. Mann, K. R. Murphy, I. J. Rae, and A. A. Chan (2012), ULF wave-driven radial diffusion simulations of the outer radiation belt, in *Dynamics of the Earth's Radiation Belts and Inner Magnetosphere*, vol. 199, edited by D. Summers et al., pp. 139–149, AGU, Washington, D. C.Geophys. Monogr. Ser., doi:10.1029/2012GM001332.
Ozeke, L. G., I. R. Mann, K. R. Murphy, I. J. Rae, and D. K. Milling (2014), Analytic expressions for ULF wave radiation belt radial diffusion coefficients, *J. Geophys. Res. Space Physics*, *119*, 1587–1605, doi:10.1002/2013JA019204.
Rae, I. J., et al. (2005), Evolution and characteristics of global Pc5 ULF waves during a high solar wind speed interval, *J. Geophys. Res.*, *110*, A12211, doi:10.1029/2005JA011007.
Rae, I. J., I. R. Mann, K. R. Murphy, L. G. Ozeke, D. K. Milling, A. A. Chan, S. R. Elkington, and F. Honary (2012), Ground-based magnetometer determination of in situ Pc4-5 ULF electric field wave spectra as a function of solar wind speed, *J. Geophys. Res.*, *117*, A04221, doi:10.1029/2011JA017335.
Reeves, G. D., K. L. McAdams, R. H. W. Friedel, and T. P. O'Brien (2003), Acceleration and loss of relativistic electrons during geomagnetic storms, *Geophys. Res. Lett.*, *30*(10), 1529, doi:10.1029/2002GL016513.
Reeves, G. D., et al. (2013), Electron acceleration in the heart of the Van Allen radiation belts, *Science*, *341*, 991–994, doi:10.1126/science.1237743.
Roederer, J. G. (1970), *Physics and Chemistry in Space. 2: Dynamics of Geomagnetically Trapped Radiation*, Springer, 166 pp., Berlin.
Sarris, T. E., and X. Li (2016), Calculating ultra-low-frequency wave power of the compressional magnetic field vs. *L* and time: Multi-spacecraft analysis using the Van Allen probes, THEMIS and GOES, *Ann. Geophys.*, *34*, 565–571, doi:10.5194/angeo-34-565-2016.
Schulz, M., and L. J. Lanzerotti (1974), *Physics and Chemistry in Space. 7: Particle Diffusion in the Radiation Belts*, Springer, 215 pp., Berlin.
Shprits, Y. Y., S. R. Elkington, N. P. Meredith, and D. A. Subbotin (2008a), Review of modeling of losses and sources of relativistic electrons in the outer radiation belt I: Radial transport, *J. Atmos. Sol. Terr. Phys.*, *70*(14), 1679–1693, doi:10.1016/j.jastp.2008.06.008.
Shprits, Y. Y., D. A. Subbotin, N. P. Meredith, and S. R. Elkington (2008b), Review of modeling of losses and sources of relativistic electrons in the outer radiation belt II: Local acceleration and loss, *J. Atmos. Sol. Terr. Phys.*, *70*(14), 1694–1713, doi:10.1016/j.jastp.2008.06.014.
Shue, J.-H., et al. (1998), Magnetopause location under extreme solar wind conditions, *J. Geophys. Res.*, *103*, 17,691–17,700, doi:10.1029/98JA01103.
Singer, H. J., L. Matheson, R. Grubb, A. Newman, and S. D. Bouwer (1996), Monitoring space weather with the GOES magnetometers, *SPIE Proc.*, *2812*, 299–308, doi:10.1117/12.254077.
Summers, D., R. M. Thorne, and F. Xiao (1998), Relativistic theory of wave-particle resonant diffusion with application to electron acceleration in the magnetosphere, *J. Geophys. Res.*, *103*, 20,487–20,500, doi:10.1029/98JA01740.
Thorne, R. M., et al. (2013), Rapid local acceleration of relativistic radiation-belt electrons by magnetospheric chorus, *Nature*, *504*, 411–414, doi:10.1038/nature12889.
Tsurutani, B. T., and W. D. Gonzalez (1994), The interplanetary causes of magnetic storms: A review, in *Magnetic Storms, Geophys. Monogr. Ser.*, vol. 98, edited by B. T. Tsurutani et al., pp. 77–89, AGU, Washington, D. C.
Turner, D. L., Y. Shprits, M. Hartinger, and V. Angelopoulos (2012), Explaining sudden losses of outer radiation belt electrons during geomagnetic storms, *Nat. Phys.*, *8*, 208–212, doi:10.1038/nphys2185.

Erratum

Louis Ozeke was inadvertently excluded from the authorship byline during the writing of this paper. In the currently published version, he has been reinstated, and this version may be considered the authoritative version of record.